

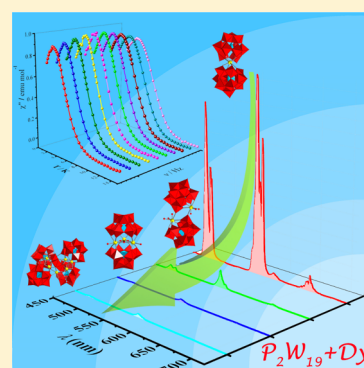
Magnetoluminescent Bifunctional Dysprosium-Based Phosphotungstates with Synthesis and Correlations between Structures and Properties

Pengtao Ma,[†] Feng Hu,[†] Yu Huo,[†] Dongdi Zhang,[†] Chao Zhang,[†] Jinyang Niu,^{*,†} and Jingping Wang^{*,†}

[†]Henan Key Laboratory of Polyoxometalate Chemistry, Institute of Molecular and Crystal Engineering, College of Chemistry and Chemical Engineering, Henan University, Kaifeng, Henan 475004, People's Republic of China

S Supporting Information

ABSTRACT: A series of dysprosium-based lacunary Keggin-type phosphotungstates have been prepared by the reaction of the preformed polyoxometalate (POM) precursor $[P_2W_{19}O_{69}(OH_2)]^{14-}$ and Dy^{3+} ions in the solution of organic carboxylic acid. Four POM-ligated lanthanide derivatives display four classes of configurations: three dimeric POMs with 2:1 type $K_2[N(CH_3)_4]_5H_4[Dy(\alpha-PW_{11}O_{39})_2] \cdot 21H_2O$ (**1Dy**), 2:2 type $Na_2[N(CH_3)_4]_4H_2[\{Dy(\alpha-PW_{11}O_{39})(H_2O)_3\}_2] \cdot 28H_2O$ (**2Dy**), and 2:3 type $K_8H_3[(DyOH_2)_3(CO_3)(\alpha-PW_9O_{34})_2] \cdot 30H_2O$ (**3Dy**), together with a tetrameric 4:8 type $K_{14}H_{12}[Dy_8(PW_{10}O_{38})_4(OH)_4(H_2O)_2(W_3O_{14})] \cdot 57H_2O$ (**4Dy**). These complexes exhibit the bifunction of luminescence and SMM properties, which indicate a bright prospect in optomagnetic devices. The solid-state fluorescence spectra of **1Dy–4Dy** all show yellowish green emission resulting from the characteristic $4f-4f$ transitions of Dy^{3+} ions. However, it is interesting that **1Dy** including only mononuclear Dy^{3+} ion has the highest luminous intensity and longest decay time in the visible or near-infrared region. Static magnetic studies reveal that **1Dy–3Dy** show the thermal depopulation of Dy^{3+} Stark sublevels, whereas **4Dy** displays the dominant ferromagnetic interactions within Dy^{3+} ions in the low temperatures as well as the thermal depopulation of Dy^{3+} Stark sublevels. The field-induced single molecule magnet (SMM) behaviors of **1Dy–4Dy** are demonstrated by dynamic magnetic studies.



INTRODUCTION

Lanthanide (Ln)-based crystalline materials as one of the most important area in industrial manufacture have drawn more and more attention because of excellent luminescence and magnetic properties and promising applications in large scale memory devices, optical switches, optoelectronic devices, smart devices, and so on.^{1–4} Ln ions possess sharp emissions and long excited-state lifetimes, and some Ln derivatives have admirable magnetic characteristics, for instance, single molecule magnet (SMM) behaviors.⁵ Up to now, enormous interests in Ln-based crystalline materials progressively increase because of their potential bifunctional luminescence and SMM properties. Nevertheless, it is comparatively difficult to tune the correlations between structures and properties; therefore, only few compounds with bifunctional optomagnetic properties were reported.^{6–8} The sensitization of Ln^{3+} ions will conquer the low absorption coefficient resulting from the Laporte forbidden $4f-4f$ transitions compared with the insensitive direct excitation of Ln^{3+} ions. However, the incorporation of host ligand into Ln coordination complexes leads to the occurrence of intramolecular energy transfer mediated by ligand-to-metal charge-transfer (LMCT) named as the antenna effect, which will improve the fluorescent characteristics. Therefore, it is highly appealing to find an appropriate host

ligand with synergistic effect to build the novel multifunctional Ln-based crystalline materials.

Polyoxometalates (POMs) are a class of polynuclear metal oxide clusters composed of early transition-metal centered MO_n polyhedra with corner-, edge-, or face-sharing modes.⁹ They displays flexible coordination modes, versatile structural topologies, oxidative stability, and remarkable electronic properties, which enable them to have the potential in magnetism, luminescence, Lewis acid catalytic activity, etc.^{10–12} Lacunary POMs have more active coordination sites with respect to plenary POMs and favor to bind with oxophilic Ln^{3+} ions. Therefore, there are lots of Ln-substituted lacunary POMs (LSLPs) have been reported so far, but these compounds possessing outstanding luminescence properties are seldom found.^{13–16} Wang et al. prepared the photoluminescent multilayer films using $K_{12}[EuP_5W_{30}O_{110}]$ precursor by the self-assembly method.¹³ Later, Wu's group synthesized a transparent luminescent hybrid material using $Na_9EuW_{10}O_{36} \cdot 32H_2O$ precursor.¹⁴ Recently, Boskovic et al. reported two new structurally related Tb-based POM derivatives $[Tb_2(pic)-$

Received: December 28, 2016

Revised: February 17, 2017

Published: February 22, 2017

$(\text{H}_2\text{O})_2(\text{B}-\beta\text{-AsW}_8\text{O}_{30})_2(\text{WO}_2(\text{pic}))_3]^{10-}$ and $[\text{Tb}_8(\text{pic})_6(\text{H}_2\text{O})_{22}(\text{B}-\beta\text{-AsW}_8\text{O}_{30})_4(\text{WO}_2(\text{pic}))_6]^{12-}$ with discrepant luminescence behaviors resulting from four different terbium coordination environments.¹⁵ Very recently, Zhao et al. synthesized three noncentrosymmetric tunable photoluminescent Ln-based POMs solids $\{[\text{Ln}_2(\text{DMF})_8(\text{H}_2\text{O})_6]-[\text{ZnW}_{12}\text{O}_{40}]\}_4\text{DMF}$ (Ln = La^{3+} , Eu^{3+} , and Tb^{3+}), which are fine-tuned by changing the ratios of Ln^{3+} ions.¹⁶ In these compounds, POMs ligands as mediums sensitizing Ln^{3+} ions emission implement the photoexcitation of the $\text{O} \rightarrow \text{W}$ LMCT, thus leading to the more effective intramolecular energy transfer from POMs $\text{O} \rightarrow \text{W}$ excited state to the lowest excited state of Ln^{3+} fluorescent centers, which have been comprehensively studied by Yamase and co-workers.^{17,18} More than that, lacunary POMs as multidentate inorganic ligands can provide different coordination configurations and symmetries for Ln^{3+} ions, which will reduce the possibility of the luminescence quenching caused by the coordination of Ln^{3+} ions with aqua or similar ligands.

SMMs possessing favorable applications in high-density storage devices and spintronics have been widely found in recent years.^{19–21} It is vitally important to choose metal centers that both have the large magnetic anisotropy and ground-state spin for the synthesis of SMMs, but two factors cannot acquire together from previous work because the magnetic anisotropy decrease with the increase of the ground-state spin.²² Ln^{3+} ions are appropriate candidates to incorporate host ligands with the aim of developing SMMs with high anisotropy barriers, which have more unpaired electrons and large spin–orbit coupling effect. Particularly, the Dy-based SMMs display the intriguing behaviors stemming from the noncollinearity of the magnetization easy axes, and Dy^{3+} is a Kramer ion (${}^6\text{H}_{15/2}$, $g_J = 4/3$) with the large magnetic anisotropy.²³ Thereby, some Ln complexes behaving as SMMs have been recorded for the past few years, but POM-based SMMs are just in the infancy. It seems interesting to study the POM-based SMMs because POMs can act as promising supporting ligands for SMMs, which ensure magnetic insulation of Ln^{3+} ions and thus minimize dipole–dipole coupling interactions between adjacent molecules depending on their steric bulk. The first LSLP SMM is $[\text{ErW}_{10}\text{O}_{36}]^{9-}$ that was reported by Coronado et al., which affords a barrier (U_{eff}/k_B) of 55.2 K with a relaxation time (τ_0) of 1.6×10^{-8} s.²⁴ In 2011, Boskovic et al. utilized the adaptive $[\text{As}_2\text{W}_{19}\text{O}_{67}(\text{H}_2\text{O})]^{14-}$ precursor to prepare a series of LSLPs (HDABCO) $_8\text{H}_3\text{Li}_8[\text{Ln}_4\text{As}_2\text{W}_{40}\text{O}_{144}(\text{H}_2\text{O})_{10}(\text{gly})_2] \cdot 25\text{H}_2\text{O}$, in which the Dy-based derivative is the first multi-Ln-containing POM-based SMM.²⁵ In the following year, Cardona-Serra et al. discovered the mononuclear Ln complexes $[\text{LnP}_3\text{W}_{30}\text{O}_{110}]^{12-}$ with a 5-fold symmetry, where the Dy- and Ho-based derivatives present slowing relaxation of magnetization.²⁶ Subsequently, Suzuki et al. developed a switchable SMM system by reversible transformation of dinuclear Dy cores in POMs with 65.7 K energy barrier and 1.6×10^{-8} s relaxation time.²⁷

Our group is also intensively interested in exploring optomagnetic bifunctional Ln-based crystalline materials by using POM host ligands, thus we launched on the exploration of lacunary POMs with Ln salts for preparing multifunctional crystalline solid materials. In 2015, we discovered a series of tri-Ln encapsulated arsenotungstates $[\text{Ln}_3(\mu_3\text{-OH})(\text{H}_2\text{O})_8(\text{AsW}_9\text{O}_{33})(\text{AsW}_{10}\text{O}_{35}(\text{mal}))]_2^{22-}$ (Ln = Dy^{3+} , Tb^{3+} , Gd^{3+} , Eu^{3+} , and Sm^{3+}) using the $[\text{As}_2\text{W}_{19}\text{O}_{67}(\text{H}_2\text{O})]^{14-}$ precursor,²⁸ in which the Dy-based derivative shows

fluorescence and SMM properties. Very recently, we utilized the $[\text{P}_2\text{W}_{19}\text{O}_{69}(\text{H}_2\text{O})]^{14-}$ precursor and isolated a new series of double-tartaric bridging mono-Ln substituted phosphotungstates $[\text{Ln}(\text{C}_4\text{H}_2\text{O}_6)(\alpha\text{-PW}_{11}\text{O}_{39})]_2^{16-}$ (Ln = Dy^{3+} , Er^{3+} , and Yb^{3+}), where the Dy-based derivative displays reversible photochromic, switchable luminescence, and SMMs properties.²⁹ Actually, the $[\text{P}_2\text{W}_{19}\text{O}_{69}(\text{H}_2\text{O})]^{14-}$ is metastable dilacunary precursor similar to $[\text{As}_2\text{W}_{19}\text{O}_{67}(\text{H}_2\text{O})]^{14-}$, which can be transformed to various building blocks (such as $[\alpha\text{-PW}_{11}\text{O}_{39}]^{6-}$, $[\alpha\text{-PW}_{10}\text{O}_{38}]^{10-}$, and $[\alpha\text{-PW}_9\text{O}_{34}]^{9-}$).^{30,31} Herein, we focused on this system of the $[\text{P}_2\text{W}_{19}\text{O}_{69}(\text{H}_2\text{O})]^{14-}$ precursor and Dy^{3+} ions, and harvested a series of Dy-based POMs derivatives from mononuclearity, binuclearity, trinuclearity to octa-nuclearity: $\text{K}_2[\text{N}(\text{CH}_3)_4]_5\text{H}_4[\text{Dy}(\alpha\text{-PW}_{11}\text{O}_{39})_2] \cdot 21\text{H}_2\text{O}$ (**1Dy**), $\text{Na}_2[\text{N}(\text{CH}_3)_4]_4\text{H}_2[\text{Dy}(\alpha\text{-PW}_{11}\text{O}_{39})(\text{H}_2\text{O})_3]_2 \cdot 28\text{H}_2\text{O}$ (**2Dy**), $\text{K}_8\text{H}_3[\text{Dy}(\text{OH})_2(\text{CO}_3)(\alpha\text{-PW}_9\text{O}_{34})_2] \cdot 30\text{H}_2\text{O}$ (**3Dy**), and $\text{K}_{14}\text{H}_{12}[\text{Dy}_8(\text{PW}_{10}\text{O}_{38})_4(\text{OH})_4(\text{H}_2\text{O})_2(\text{W}_3\text{O}_{14})] \cdot 57\text{H}_2\text{O}$ (**4Dy**), which display 2:1, 2:2, and 2:3-type dimeric and 4:8-type tetrameric structural features, respectively. It is noteworthy that these Dy^{3+} ions reside in different coordination environments, which are closely relevant with their luminescent and magnetic performances. Although **1Dy**–**4Dy** all display the yellowish green emissions resulting from the characteristic 4f–4f transition of Dy^{3+} ions, only **1Dy** presents the highest luminous intensity and the longest lifetime. The temperature-dependent magnetic susceptibilities of **1Dy**–**3Dy** indicate the dominant the depopulation of high Dy^{3+} Stark sublevels, whereas the ferromagnetic interaction between Dy^{3+} and Dy^{3+} ions within the cluster is observed for **4Dy** in the low temperature as well as the depopulation of Dy^{3+} Stark sublevels. Furthermore, the frequency dependences of the ac susceptibility for **1Dy**–**4Dy** suggest the typical field-induced SMM behaviors.

EXPERIMENTAL SECTION

Materials and Methods. All purchased chemical reagents were directly used without purification. $\text{K}_{14}[\text{P}_2\text{W}_{19}\text{O}_{69}(\text{H}_2\text{O})] \cdot 24\text{H}_2\text{O}$ was made according to the previous method.³⁰ IR spectra as KBr pellets were measured on a Bruker VERTEX 70 IR spectrometer over the range of 4000–400 cm^{-1} . Elemental analyses of carbon, nitrogen, and hydrogen were performed on an Elementar VarioElcube CHNS analyzer. The phase purity of bulk samples were further verified by powder X-ray diffraction (PXRD) patterns collected on a Bruker D8 Advance instrument with $\text{Cu K}\alpha$ radiation ($\lambda = 1.5418 \text{ \AA}$). TGA analyses were carried out on a NETZSCH STA 449 F5 analyzer under a N_2 atmosphere with $10 \text{ }^\circ\text{C}\cdot\text{min}^{-1}$ heating rate. Photoluminescence spectra and lifetime were performed on an EDINBURGH FLS980 fluorescence spectrophotometer using a 450 W xenon lamp and a μF900H microsecond flashlamp as excitation sources for the steady state and transient fluorescence measurements. Magnetic properties were investigated on a Quantum Design SQUID MPMS3 magnetometer. EDX spectra were obtained on a JSM-7610F scanning electron microscope equipped with OXFORD x-act EDS.

Synthesis of $\text{K}_2[\text{N}(\text{CH}_3)_4]_5\text{H}_4[\text{Dy}(\alpha\text{-PW}_{11}\text{O}_{39})_2] \cdot 21\text{H}_2\text{O}$ (1Dy**).** A solid sample of $\text{Dy}(\text{NO}_3)_3 \cdot 6\text{H}_2\text{O}$ (0.26 g, 0.57 mmol) and citric acid (0.21 g, 1.00 mmol) were dissolved in 30 mL of distilled water under stirring, then $\text{K}_{14}[\text{P}_2\text{W}_{19}\text{O}_{69}(\text{H}_2\text{O})] \cdot 24\text{H}_2\text{O}$ (1.06 g, 0.19 mmol) was added in the resulting solution with stirring. Five minutes later, the pH value of the solution was adjusted to 6.0 by NaOH ($2 \text{ mol}\cdot\text{L}^{-1}$). The mixture was vigorously stirred at $80 \text{ }^\circ\text{C}$ for 1 h. Tetramethylammonium chloride (TMACl) (0.15 g, 1.36 mmol) was dissolved into the reaction mixture with stirring for another 5 min after cooling to ambient temperature. Slow evaporation of the clear filtrate in a small beaker at the room temperature resulted in colorless block crystals of **1Dy** for around 2 weeks. Yield: 0.44 g (36.7%) based on

Table 1. Crystallographic Data of 1Dy–4Dy

	1Dy	2Dy	3Dy	4Dy
formula	C ₂₀ H ₁₀₆ DyK ₂ N ₅ O ₉₉ P ₂ W ₂₂	C ₁₆ H ₁₁₈ N ₄ Na ₂ Dy ₂ O ₁₁₂ P ₂ W ₂₂	CH ₆₉ K ₈ O ₁₀₄ P ₂ Dy ₃ W ₁₈	H ₁₃₄ NaK ₁₄ O ₂₂₃ P ₄ Dy ₈ W ₄₃
<i>M_r</i> (g mol ⁻¹)	6348.15	6636.46	5916.85	13602.31
cryst. syst.	monoclinic	triclinic	orthorhombic	triclinic
space group	<i>I</i> 2/ <i>a</i>	<i>P</i> $\bar{1}$	<i>Pnma</i>	<i>P</i> $\bar{1}$
<i>a</i> (Å)	22.406(3)	12.882(4)	34.7721(15)	20.171(5)
<i>b</i> (Å)	21.296(2)	12.991(4)	16.7381(7)	22.842(5)
<i>c</i> (Å)	51.110(6)	23.356(8)	16.3897(7)	25.871(6)
α (deg)	90	84.839(6)	90	68.211(4)
β (deg)	94.896(2)	74.434(6)	90	84.854(4)
γ (deg)	90	61.432(5)	90	84.969(4)
<i>V</i> (Å ³)	24299(5)	3303.4(18)	9539.1(7)	11005(5)
<i>Z</i>	8	1	4	2
<i>D</i> _{calcd} (g cm ⁻³)	3.341	3.194	4.142	3.883
μ (mm ⁻¹)	21.521	20.318	24.435	25.432
crystal size (mm ³)	0.41 × 0.23 × 0.18	0.38 × 0.26 × 0.25	0.22 × 0.20 × 0.18	0.38 × 0.34 × 0.29
limiting indices	-26 ≤ <i>h</i> ≤ 26 -25 ≤ <i>k</i> ≤ 23 -58 ≤ <i>l</i> ≤ 60	-15 ≤ <i>h</i> ≤ 15 -15 ≤ <i>k</i> ≤ 15 -27 ≤ <i>l</i> ≤ 23	-41 ≤ <i>h</i> ≤ 37 -19 ≤ <i>k</i> ≤ 17 -19 ≤ <i>l</i> ≤ 19	-23 ≤ <i>h</i> ≤ 24 -27 ≤ <i>k</i> ≤ 23 -30 ≤ <i>l</i> ≤ 30
No. of reflns collected	62136	17058	48152	57179
No. of independent reflns	21636	11585	8786	38906
No. of params	679	356	387	1360
GOF on <i>F</i> ²	1.042	1.027	1.052	1.023
<i>R</i> ₁ , <i>wR</i> ₂ [<i>I</i> > 2σ(<i>I</i>)]	0.0632, 0.1588	0.0767, 0.1994	0.0519, 0.1216	0.0581, 0.1439
<i>R</i> ₁ , <i>wR</i> ₂ [all data]	0.1171, 0.1970	0.1012, 0.2128	0.0782, 0.1363	0.0922, 0.1645

K₁₄[P₂W₁₉O₆₉(H₂O)]·24H₂O. Elemental analysis (%) calcd: C, 3.78; H, 1.68; N, 1.10. Found: C, 3.63; H, 1.73; N, 1.07. IR (cm⁻¹): 3431(br), 3037(w), 1616(s), 1484(s), 1104(s), 1047(s), 954(s), 891(s), 844(s), 771(w).

Synthesis of Na₂[N(CH₃)₄]₄H₂{Dy(α-PW₁₁O₃₉)(H₂O)₃]₂·28 H₂O (2Dy). The synthesis of 2Dy is similar to 1Dy except for the pH value was adjusted to 4.0. After 2 weeks, colorless block-shaped crystals of 2Dy were isolated. Yield: 0.43 g (34.2%) based on K₁₄[P₂W₁₉O₆₉(H₂O)]·24H₂O. Elemental analysis (%) calcd: C, 2.90; H, 1.79; N, 0.84. Found: C, 3.01; H, 1.80; N, 0.89. IR (cm⁻¹): 3428(br), 3043(w), 1626(s), 1484(s), 1093(s), 1051(s), 954(s), 890(s), 824(s), 698(w).

Synthesis of K₈H₃[(DyOH)₂(CO₃)(α-PW₉O₃₄)₂]₂·30H₂O (3Dy). The synthesis process of 3Dy is similar to 1Dy except that citric acid was replaced by malic acid (0.20 g, 1.50 mmol). In addition, the pH value of this reaction mixture was adjusted to 7.1 by KOH (2 mol·L⁻¹). Colorless transparent crystals of 3Dy were obtained in 1 week. Yield: 0.29 g (27.3%) based on K₁₄[P₂W₁₉O₆₉(H₂O)]·24H₂O. Elemental analysis (%) calcd: C, 0.20; H, 1.18. Found: C, 0.22; H, 1.29. IR (cm⁻¹): 3430 (br), 1628 (s), 1478 (s), 1063(s), 1015 (s), 940 (s), 828 (s), 778 (s), 705 (w).

Synthesis of K₁₄H₁₂[Dy₈(PW₁₀O₃₈)₄(OH)₄(H₂O)₂(W₂O₁₄)]·57H₂O (4Dy). The reaction process of 4Dy is also similar to 3Dy except that Dy(NO₃)₃·6H₂O (0.26 g, 0.57 mmol) was replaced by DyCl₃·6H₂O (0.27 g, 0.72 mmol). In addition, the pH value of this reaction mixture was adjusted to 7.3 by KOH (2 mol·L⁻¹), then the resulting solution was vigorously stirred at 60 °C for 1 h. Finally, colorless block-shaped crystals of 4Dy were afforded. Yield: 0.32 g (41.5%) based on K₁₄[P₂W₁₉O₆₉(H₂O)]·24H₂O. IR (cm⁻¹): 3413(br), 1617(s), 1088(s), 1052(s), 1027(s), 953(s), 896(w), 815(s), 768(w).

X-ray Crystallography. X-ray single-crystal diffraction intensity data of 1Dy–4Dy were collected on a Bruker APEX2 CCD diffractometer equipped with graphite-monochromated Mo *K* α radiation ($\lambda = 0.71073$ Å) at 296 K. Multiscan absorption correction and Lorentz polarization was applied relying on the SADABS software package. Direct method was applied for all these original structures, in which all the heavy atom positions (Dy and W) were readily located and the other non-hydrogen (K, Na, P, C, N, and O) atoms were

subsequently determined by the difference Fourier maps. Full-matrix least-squares structure refinements against *F*² were performed using the SHELXTL crystallographic program.³² During the refinement of last cycles, all heavy elements included P, Dy, and W atoms were anisotropically refined; whereas all other non-hydrogen atoms (C, N, and O) were isotropically refined. Anisotropic thermal parameters for K and Na cations were anisotropically refined, and highly disordered cations were isotropically refined using isotropic thermal parameters. The numbers of lattice water components were calculated on the basis of TGA analysis. H atoms on TMA groups were fixed in calculated positions. The hydrogen atoms from solvent water were added in the formula directly. In all these compounds, the structures contain large solvent accessible voids, which is due to the fact that segmental alkali cations (K or Na) and water molecules of hydration are significantly disordered, and this is usually observed in POMs crystallography. The detailed crystallographic data and structure refinements are listed in Table 1. Crystallographic data in this article have been deposited in the Cambridge Crystallographic Data Centre with CCDC 1521758–1521761 for 1Dy–4Dy, respectively. These data can be obtained free of charge from The Cambridge Crystallographic Data Centre via www.ccdc.cam.ac.uk/data_request/cif.

RESULTS AND DISCUSSION

Synthesis. In the past several decades, a good deal of LSLPs derivatives has been constantly recorded; most are prepared from lacunary Keggin or Dawson precursors,^{33–36} while the LSLP derivatives synthesized by the dilacunary precursor [P₂W₁₉O₆₉(H₂O)]¹⁴⁻ are seldom recorded.^{29,37,38} Synchronously, inspired by the fact of abundant and various Ln-containing arsenotungstate derivatives obtained by the adaptable precursor [As₂W₁₉O₆₇(H₂O)]¹⁴⁻, we have launched exploration of this reaction system between the precursor [P₂W₁₉O₆₉(H₂O)]¹⁴⁻ and Ln³⁺ ions with the aim of discovering much more LSLPs derivatives with various configurations of Ln³⁺ ions, which will facilitate the exploration of the correlations between the structures and their performances. However, the preparation of new LSLPs using

$[P_2W_{19}O_{69}(H_2O)]^{14-}$ precursor has been a great challenge because the combination of oxyphilic Ln^{3+} ions with dilacunar $[P_2W_{19}O_{69}(H_2O)]^{14-}$ precursor easily leads to amorphous precipitates instead of crystallization, and Ln^{3+} ions in the $[P_2W_{19}O_{69}(H_2O)]^{14-}$ reaction system are easy to hydrolyze with water, which brings a great difficulty to manufacturing functionalized LSLPs. In order to overcome these obstacles, we utilize organic carboxylic acids as protective agents or functionalized ligands to capture Ln^{3+} ions in the process of coordination assembly, which can effectively prevent the hydrolysis of Ln^{3+} ions.

In the case of the structure, very similar to the dilacunar precursor $[As_2W_{19}O_{67}(H_2O)]^{14-}$, the bridging $\{WO(H_2O)\}$ connector in the precursor $[P_2W_{19}O_{69}(H_2O)]^{14-}$ links two $[\alpha-PW_9O_{34}]^{9-}$ subunits, meanwhile, which presents a vulnerable fracture point where it can be disassembled in various fragments. However, it is obviously different from the fact that the adaptable precursor $[As_2W_{19}O_{67}(H_2O)]^{14-}$ can produce $\{B-\alpha-AsW_{10}O_{35}\}$, $\{B-\alpha-AsW_9O_{33}\}$, $\{B-\beta-AsW_9O_{33}\}$, and $\{B-\beta-AsW_8O_{29}(OH)\}$ building blocks; the metastable polyanion $[P_2W_{19}O_{69}(H_2O)]^{14-}$ can form lacunar Keggin-type $[\alpha-PW_{11}O_{39}]^{6-}$, $[\alpha-PW_{10}O_{38}]^{10-}$ and $[\alpha-PW_9O_{34}]^{9-}$ species only because of the discrepancy of the central heteroatoms. It is noteworthy that, these highly active fragments $[\alpha-PW_{11}O_{39}]^{6-}$, $[\alpha-PW_{10}O_{38}]^{10-}$, and $[\alpha-PW_9O_{34}]^{9-}$ are derived from the dissociation and recombination of the $[P_2W_{19}O_{69}(H_2O)]^{14-}$ precursor under specific conditions (Figure 1), which increase the diversities of targeted

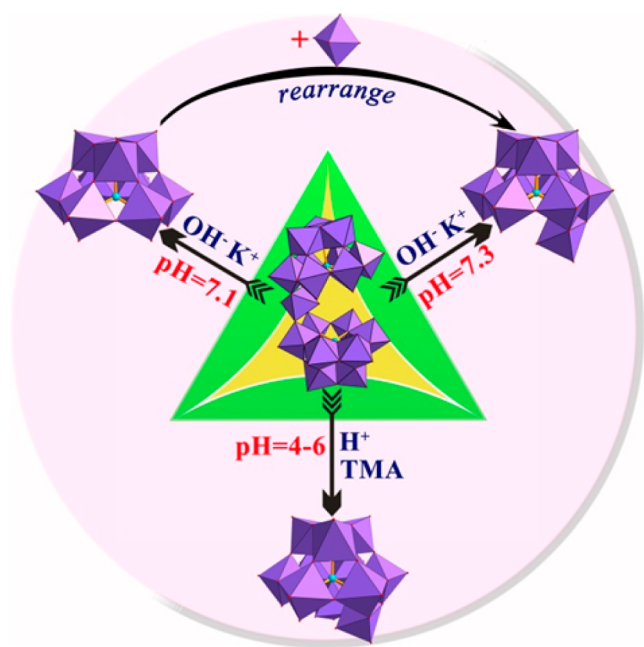


Figure 1. Conversion of parent compound $[P_2W_{19}O_{69}(OH)_2]^{14-}$ into three classic Keggin units $[\alpha-PW_{11}O_{39}]^{7-}$, $[\alpha-PW_{10}O_{38}]^{11-}$, and $[\alpha-PW_9O_{34}]^{9-}$ in the aqueous solution under different conditions.

LSLP materials. As we know, $[P_2W_{19}O_{69}(H_2O)]^{14-}$ is relatively stable in the condition of high concentration of K^+ ions, which is prone to be transformed to $[\alpha-PW_{11}O_{39}]^{6-}$ in the absence of K^+ counteraction or in a minor amount of K^+ counteraction.³⁰ Furthermore, $[P_2W_{19}O_{69}(H_2O)]^{14-}$ is also restructured into $[\alpha-PW_{11}O_{39}]^{6-}$ in the slight excess of TMA cations. Therefore, the $[P_2W_{19}O_{69}(H_2O)]^{14-}$ precursor is inclined to convert into

monolacunar Keggin-type $[\alpha-PW_{11}O_{39}]^{6-}$ fragment under acidic pH environments in the presence of abundant TMA cations, yet the architectural difference of **1Dy** and **2Dy** can be attributable to the different assembly environments (pH = 6.0 for **1Dy** and 4.0 for **2Dy**) for the system. On the contrary, the $[P_2W_{19}O_{69}(H_2O)]^{14-}$ precursor can easily be degraded into the $[\alpha-PW_9O_{34}]^{9-}$ and/or $[\alpha-PW_{10}O_{38}]^{10-}$ moieties (even the trivacant Keggin fragment $[\alpha-PW_9O_{34}]^{9-}$ can be rearranged to dilacunar $[\alpha-PW_{10}O_{38}]^{10-}$ unit) in the presence of K^+ ions in a neutral or weak basic medium (pH \geq 7.0).³⁸ Thus, the dilacunar $[P_2W_{19}O_{69}(H_2O)]^{14-}$ precursor is isomerized into the $[\alpha-PW_9O_{34}]^{9-}$ for the assembly of **3Dy** and $[\alpha-PW_{10}O_{38}]^{10-}$ for the combination of **4Dy**. In addition, another interesting discovery is that **3Dy** was synthesized without addition of Na_2CO_3 in the reaction, yet the tridentate template ligand CO_3^{2-} generated in situ from the decarboxylic reaction of malic acid in the temperature of 80 °C. This method is distinctly different from the synthetic strategy of Francesconi and co-workers, where the template agent CO_3^{2-} was directly added in the reaction system.^{33,39} However, similar phenomenon was observed from the previous research of $[Dy_{3-n}K_n(H_2O)_3(CO_3)(A-\alpha-AsW_9O_{34})(A-\beta-AsW_9O_{34})]^{40}$.

Structural Description. Single-crystal structural analyses indicated that **1Dy**–**4Dy** crystallize in the monoclinic $I2/a$, the triclinic $P\bar{1}$, the orthorhombic $Pnma$, and the triclinic $P\bar{1}$ space groups, respectively, which display 2:1, 2:2, and 2:3-type dimeric and 4:8-type tetrameric polyanion structures, respectively. The polyanion of **1Dy** consists of two monolacunar $[\alpha-PW_{11}O_{39}]^{7-}$ building blocks joined together by a Dy^{3+} ion (Figure 2a), whereas the polyanion of **2Dy** is composed of two $[\alpha-PW_{11}O_{39}]^{7-}$ units linked together through two $\{Dy(H_2O)_3\}$ bridges (Figure 2b). As for **3Dy**, its polyanion contains a trinuclear $\{Dy_3(CO_3)(H_2O)_3\}$ cluster sandwiched by two $[\alpha-PW_9O_{34}]^{9-}$ units (Figure 2c). In the $\{Dy_3(CO_3)(H_2O)_3\}$ cluster, the carbonate ion templates three Dy^{3+} ions forming a planar triangle. With regard to **4Dy**, it can be viewed as a tetrameric polyanion built by four bi- Dy^{3+} substituted Keggin-type fragments linked by three additional tungstate units (Figure 2d). Above-mentioned results indicate the assembly of the $[P_2W_{19}O_{69}(H_2O)]^{14-}$ precursors and Dy^{3+} ions under different conditions can effectively lead to great structural varieties of POM-based Dy^{3+} derivatives (Figure 2 and Figure S1, Supporting Information).

Apart from the structural diversity of POM-based Ln derivatives, we pay close attention to the coordination configurations of Ln^{3+} ions, which may be the immanent cause of the correlations between structures and properties. Therefore, the configurations of Dy^{3+} ions in **1Dy**–**4Dy** are discussed in detail (Figure 2e). The Dy^{3+} ions of **1Dy** and **2Dy** are all eight-coordinate, which all display distorted square antiprism configurations. It is of note that the eight-coordinate Dy^{3+} ion in **1Dy** is chelated by eight oxygen atoms entirely provided by two $[\alpha-PW_{11}O_{39}]^{7-}$ units, whereas each Dy^{3+} ions in **2Dy** is bonded by five O atoms from two $[\alpha-PW_{11}O_{39}]^{7-}$ units and three water ligands (O1W, O2W, O3W). The three Dy^{3+} ions in **3Dy** all adopt seven-coordinate monocapped triangular prism geometries, which are all combined with four O donors from two $[\alpha-PW_9O_{34}]^{9-}$ units, two O atoms of the carbonate ion, and a coordinated water ligand (O1W). Furthermore, there are two kinds of configurations of Dy^{3+} ions found in **4Dy**, where eight-coordinate square antiprism and seven-coordinate monocapped triangular prism geometries coexist in the polyanion. The eight-coordinate Dy^{3+} ions in **4Dy**

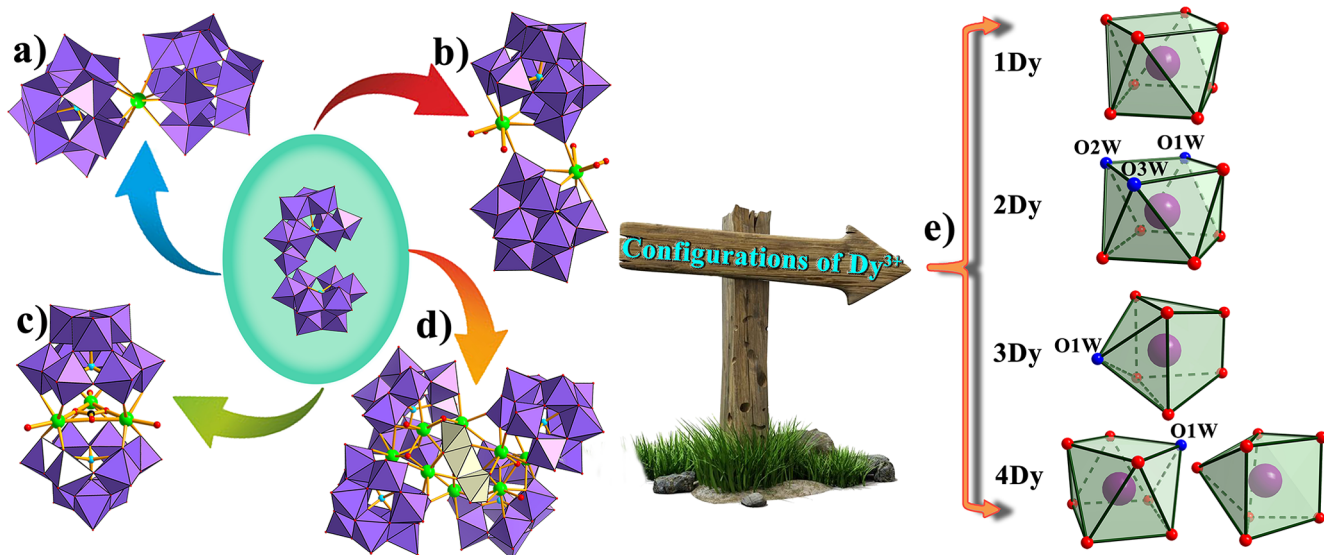


Figure 2. Polyhedral representation of 1Dy (a), 2Dy (b), 3Dy (c), and 4Dy (d). (Color code: WO_6 , purple octahedra; P, cyanine; Dy, green; O, red; C, black). (e) Coordination configurations of Dy^{3+} ions in the 1Dy–4Dy. The red and blue spheres represent the O atoms provided by POMs units and water ligands, respectively.

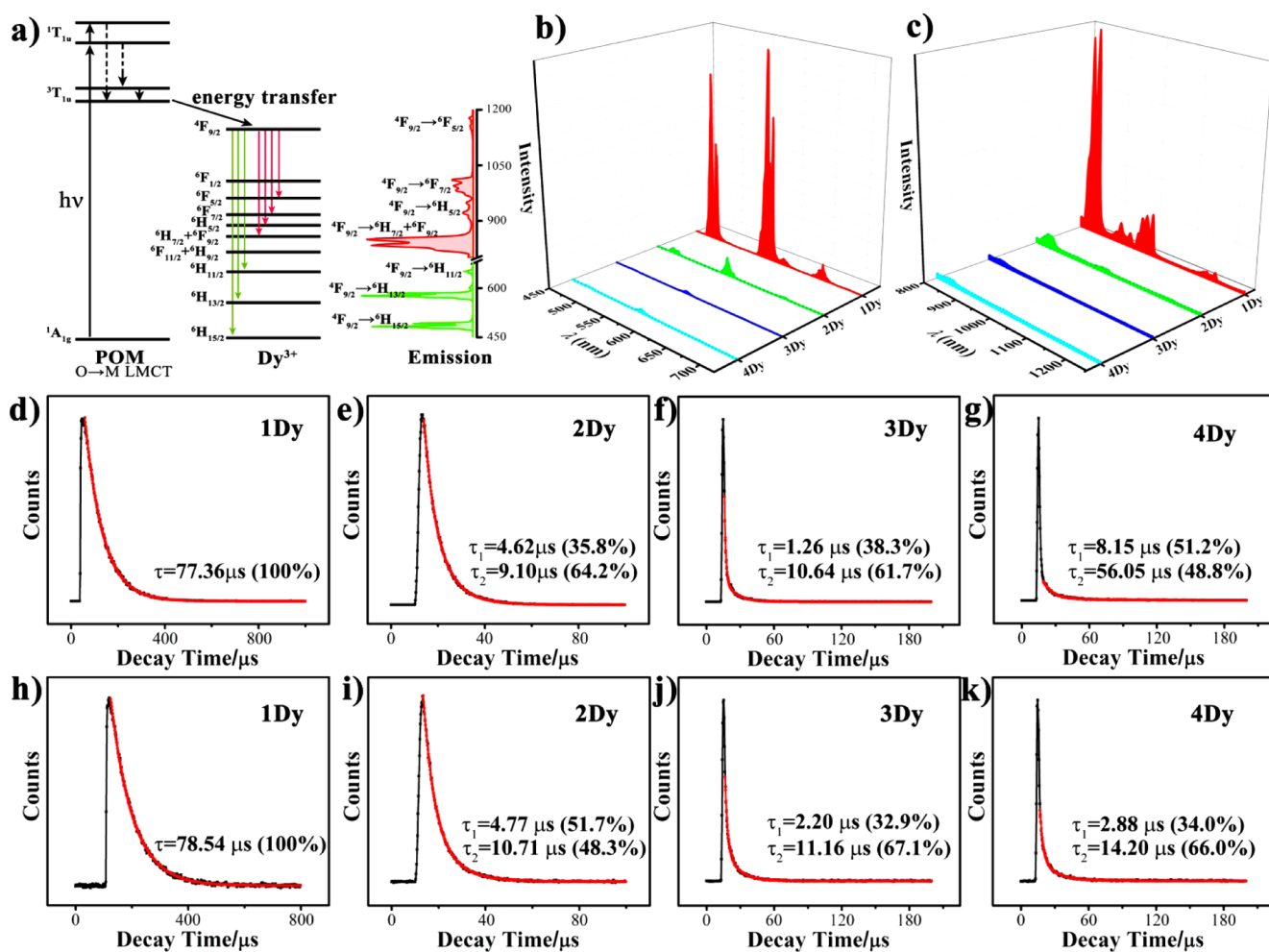


Figure 3. (a) Schematic representation of energy transfer processes for Dy^{3+} ions and the visible together with NIR emissions in 1Dy–4Dy. (b) Emission spectra in the visible region (366 nm excitation) of 1Dy–4Dy. (c) Emission spectra in the NIR region (366 nm excitation) of 1Dy–4Dy. (d–g) The visible emission decay curves of 1Dy–4Dy. (h–k) The NIR emission decay curves of 1Dy–4Dy.

are bonded by seven oxygen atoms from POMs fragments and one water ligand (O1W), while the seven-coordinate Dy^{3+} ions in **4Dy** are all completed by seven oxygen atoms from POMs fragments.

Photoluminescence Properties. In general, Ln-based luminescent materials have aroused extensive interest due to the high color purity and the narrow emission lines originating from characteristic intra- $4f-4f$ transitions of Ln^{3+} cations, thus leading to their various applications in lighting and light conversion technologies in areas, for example, displays, sensors, lasers, optical data storage, light-emitting diodes, and optical switching devices.^{41,42} Moreover, the luminescence emissions of Ln-based POM materials rely heavily upon the intrinsic properties of POM hosts, local symmetry, and coordination environments of Ln^{3+} ions, together with the number of the coordinated aqua coligands with Ln^{3+} centers, where the structural and compositional versatility can also be tuned by the structural assembly by means of the sensitization or quenching effect of the hosts.^{15,43} In Ln-based POM phosphors, the photosensitization primarily refers to the population of the triplet excited states of POMs hosts, which allows efficient energy transfer from POM $\text{O} \rightarrow \text{W}$ LMCT excited state to Ln^{3+} luminescence centers, then the Ln^{3+} ions with different energy levels emit visible and/or NIR light on account of the transition of lowest excited states to ground state multiplets (Figure 3a). Therefore, photoluminescence properties of the solid-state samples of **1Dy–4Dy** have been investigated under the same conditions in order to find out the internal correlations of structures and fluorescence properties.

In these Dy-based POM materials, the photoexcitation of POM $\text{O} \rightarrow \text{W}$ LMCT furnishes the fluorescence-emission from the ${}^4\text{F}_{9/2}$ excited state of the Dy^{3+} component to ${}^6\text{H}_j$ ($J = 15/2, 13/2, 11/2,$ and $7/2$), ${}^6\text{H}_{7/2} + {}^6\text{F}_{9/2}$ and ${}^6\text{F}_j$ ($J = 5/2$ and $3/2$) ground state multiplets (Figure 3a). Upon direct UV irradiation ($\lambda_{\text{max}} = 366$ nm) (Figure S2a, Supporting Information), the $4f-4f$ transition of Dy^{3+} ions in **1Dy–4Dy** all cause yellowish green luminescence in the visible region, which all present three major characteristic emission peaks located at 479, 573, and 662 nm, respectively (Figure 3a,b). Two strong peaks appearing at 479 and 662 nm are assigned to the ${}^4\text{F}_{9/2} \rightarrow {}^6\text{H}_{15/2}$ and ${}^4\text{F}_{9/2} \rightarrow {}^6\text{H}_{11/2}$, in which the magnetic dipole transition ${}^4\text{F}_{9/2} \rightarrow {}^6\text{H}_{15/2}$ is insensitive to the symmetry of crystal field and the local coordination environment around the Dy^{3+} ions. On the contrary, the strongest signal at 573 nm is attributed to the electric dipole transition ${}^4\text{F}_{9/2} \rightarrow {}^6\text{H}_{13/2}$, which is hypersensitive to the local environments and crystal fields around Dy^{3+} ions. In the case that the Dy^{3+} ions situate in the low symmetry environments, the transition ${}^4\text{F}_{9/2} \rightarrow {}^6\text{H}_{13/2}$ is usually dominant in the emission spectrum.^{44,45} Obviously, the luminescent intensity of the electric dipole transition ${}^4\text{F}_{9/2} \rightarrow {}^6\text{H}_{13/2}$ is much higher than that of the magnetic dipole transition ${}^4\text{F}_{9/2} \rightarrow {}^6\text{H}_{15/2}$ in the emission spectra of **1Dy–4Dy** (Figure 3a,b), illustrating that all the Dy^{3+} ions situate in the low symmetrical environments without inversion, which are consistent with the distorted square antiprismatic or monocapped triangular prism geometries of Dy^{3+} ions in **1Dy–4Dy**.

When **1Dy–4Dy** were excited under the same ultraviolet light of 366 nm (Figure S2b, Supporting Information), the NIR photoluminescence spectra were observed with four characteristic emission bands of Dy^{3+} ions with maxima at 864, 888, 997, and 1123 nm (Figure 3a,c), which are attributed to the transitions from ${}^4\text{F}_{9/2}$ to ${}^6\text{H}_{7/2} + {}^6\text{F}_{9/2}$, ${}^6\text{H}_{7/2}$, ${}^6\text{F}_{5/2}$, and ${}^6\text{F}_{3/2}$, respectively. Simultaneously, there are many cleavages of the

NIR emission peaks as well as the visible emission signals due to the prominent crystal-field splitting.⁴⁶

It is noteworthy that the luminous intensity of **1Dy** among the **1Dy–4Dy** is highest regardless of the visible or NIR emission (Figure 3b,c), although the percent content of Dy^{3+} component in mononuclear **1Dy** is lowest among **1Dy–4Dy**. Comparatively, the luminous intensity sequence among the **1Dy–4Dy** from high to low is **1Dy** \gg **2Dy** $>$ **4Dy** $>$ **3Dy** (Figures 3b,c and S3a,b, Supporting Information), which has the close relationship with the local symmetry and the coordination geometries of Dy^{3+} ions, together with the number of aqua coligands in **1Dy–4Dy**. Structure analysis shows that the Dy^{3+} ion in **1Dy** adopts the eight-coordinate distorted square antiprism configuration and does not have any coordinated water molecule among **1Dy–4Dy**. In addition, **3Dy** and **4Dy** comprise some Dy^{3+} ions with seven-coordinate monocapped triangular prism geometry, which obviously has lower symmetry than that of the one with the eight-coordinate square antiprism configuration. As it stands, the Ln-containing compounds will have lower luminous intensity if the Ln ions connect with coordinated water molecules that cause fluorescent quenching because the high frequency O–H oscillator prevents the $4f-4f$ transition.⁴⁷ As a result, **1Dy** displays the strongest fluorescence, while the luminous intensity of **2Dy** is also clearly higher than that of **3Dy** and **4Dy**, indicating that the energy transfer from inorganic POM components to Dy^{3+} ions with eight-coordinate square antiprism geometry is more effective than to Dy^{3+} ions with seven-coordinate monocapped triangular prism configuration. Comparing the emissions of **3Dy** and **4Dy**, the luminous intensity of **4Dy** is little higher than that of **3Dy** maybe because **4Dy** has both eight-coordinate square antiprism and seven-coordinate monocapped triangular prism configurations. Therefore, the results indicate that (1) the aqua coligands coordinating to the Dy^{3+} ion can lead to fluorescence quenching and that (2) the luminescence of the Dy^{3+} ion with seven-coordinate monocapped triangular prism configuration is poorly sensitized compared to that of eight-coordinate square antiprism geometry.

Measurements of the fluorescence lifetime afford the decay of the ${}^6\text{H}_{13/2}$ visible luminescence at 573 nm and ${}^6\text{H}_{7/2} + {}^6\text{F}_{9/2}$ NIR luminescence (excited at 366 nm). The luminescence decay curves of **1Dy–4Dy** are shown in Figure 3d–k and are well fitted with the exponential function. For **1Dy**, the visible luminescence decay curve (Figure 3d) is fitted well with the monoexponential function and yields a lifetime of $\tau = 77.36$ μs (100%), which displays the long lifetime luminescence among the most Dy-based complexes.⁴⁸ As for **2Dy–4Dy**, their visible luminescence decay curves (Figure 3e–g) are in good fitness with a biexponential function $I = A_1 \exp(-t/\tau_1) + A_2 \exp(-t/\tau_2)$, providing lifetimes of $\tau_1 = 4.62$ μs (35.8%), $\tau_2 = 9.10$ μs (64.2%) for **2Dy**; $\tau_1 = 1.26$ μs (38.3%), $\tau_2 = 10.64$ μs (61.7%) for **3Dy**; and $\tau_1 = 8.15$ μs (51.2%), $\tau_2 = 56.05$ μs (48.8%) for **4Dy**. The NIR lifetimes of **1Dy–4Dy** are also detected as well as the decays of visible emission at ambient temperature (Figure 3h–k), given that the NIR lifetimes are very similar to the visible luminescence lifetimes. The lifetime of **1Dy** is longest with $\tau = 78.54$ μs (100%) fitted in monoexponential decay, whereas the lifetimes of **2Dy–4Dy** fitted in biexponential decay are also relatively short (**2Dy** ($\tau_1 = 4.77$ μs (51.7%), $\tau_2 = 10.71$ μs (58.3%)), **3Dy** ($\tau_1 = 2.20$ μs (32.9%), $\tau_2 = 11.16$ μs (66.1%)), and **4Dy** ($\tau_1 = 2.88$ μs (34.0%), $\tau_2 = 14.20$ μs

(66%). Obviously, 1Dy displays the longest lifetime among 1Dy–4Dy whether it is visible or NIR luminescence.

Magnetic Properties. Variable-temperature magnetic susceptibilities of 1Dy–4Dy were measured with an applied dc field 1000 Oe in the temperature range 1.8–300 K. As shown in Figure 4a, the $\chi_M T$ value at room temperature of 14.5

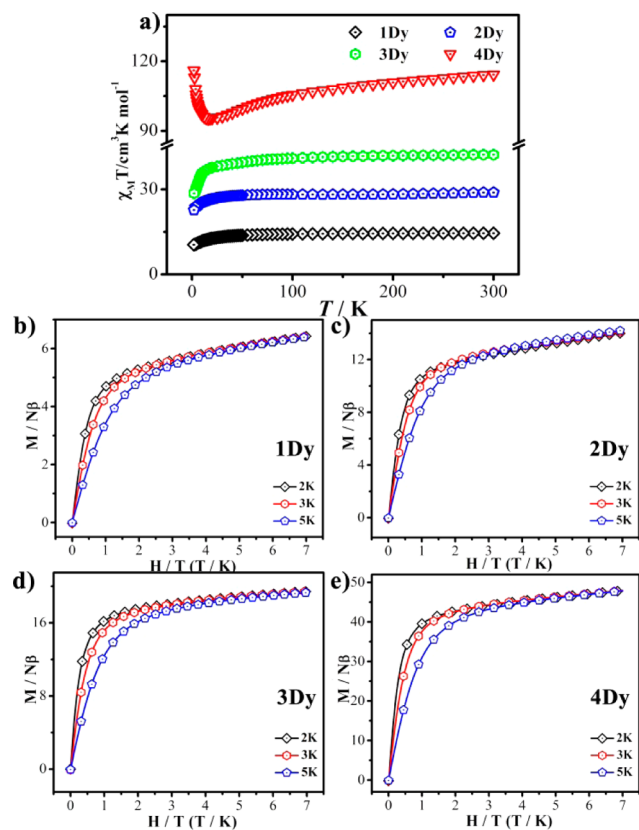


Figure 4. (a) Temperature-dependent $\chi_M T$ curves for 1Dy–4Dy at 1000 Oe. Field-dependent magnetization curves in the form of M vs H/T between 2–5 K for 1Dy (b), 2Dy (c), 3Dy (d), and 4Dy (e).

$\text{cm}^3 \text{K mol}^{-1}$ for 1Dy is slightly higher than the noninteracting value of one Dy^{3+} ion of $14.2 \text{ cm}^3 \text{K mol}^{-1}$ (${}^6\text{H}_{15/2}$, $g = 4/3$) and decreases to $10.7 \text{ cm}^3 \text{K mol}^{-1}$ at 1.8 K. For 2Dy, the $\chi_M T$ value of $28.9 \text{ cm}^3 \text{K mol}^{-1}$ at 300 K is well consistent with two uncoupled Dy^{3+} ions of $28.3 \text{ cm}^3 \text{K mol}^{-1}$ and gradually drops to $16.1 \text{ cm}^3 \text{K mol}^{-1}$ at 1.8 K. With regard to 3Dy, the room-temperature $\chi_M T$ value of $42.3 \text{ cm}^3 \text{K mol}^{-1}$ is close to the theoretical value of three spin-only Dy^{3+} ions.

Upon cooling, the $\chi_M T$ value gradually decreases until approximately 20 K, and then sharply declines to the minimum of $28.6 \text{ cm}^3 \text{K mol}^{-1}$ at 1.8 K. As is well-known, the magnetic behavior that these $\chi_M T$ values for 1Dy–3Dy generally decline as the temperature dropped mainly because of the thermal depopulation of the excited Stark sublevels of Dy^{3+} ions under crystal-field splitting or the combination with weak $\text{Dy}^{3+}\cdots\text{Dy}^{3+}$ antiferromagnetic interactions.⁴⁹ As for 4Dy, the room-temperature $\chi_M T$ value of $114.3 \text{ cm}^3 \text{K mol}^{-1}$ is also close to the expected value ($113.4 \text{ cm}^3 \text{K mol}^{-1}$) of eight uncoupled Dy^{3+} ions with a ground state of ${}^6\text{H}_{15/2}$. The $\chi_M T$ value first undergoes a slow drop between 300 and 16 K and reaches the lowest level of $95.3 \text{ cm}^3 \text{K mol}^{-1}$ at 16 K as a result of the progressive thermal depopulation of Dy^{3+} Stark sublevels,⁵⁰ and then the $\chi_M T$ value rapidly rises below 16 K and reaches its

peak value of $116.1 \text{ cm}^3 \text{K mol}^{-1}$ at 1.8 K. This magnetic behavior at low temperature is possibly subjected to dominant ferromagnetic interactions within Dy^{3+} ions or occupations of Stark sublevels.

The field-dependent magnetizations for 1Dy–4Dy measured in 2–5 K display a fast rise below 1 T and then increase gently in the range of 1–7 T, which are all far lower than their saturation values up to a field of 7 T (Figure 4b–e). The magnetization values of 1Dy–4Dy in the high magnetic field of 7 T at 2 K are 6.4, 14.0, 21.8, and $47.9 \text{ N}\beta$, respectively, which are far less than the theoretical saturation value. This absence of magnetic saturation indicates the existence of a significant magnetic anisotropy and/or low lying excited states of Dy^{3+} ions. Additionally, the nonoverlapping of the curves of magnetization versus magnetic field below 5 K also displays the presence of a prominent magnetic anisotropy of Dy^{3+} ions.

For the purpose of exploring dynamic magnetic behaviors, alternating-current (ac) susceptibility measurements are undertaken for 1Dy–4Dy in different magnetic fields, which indicate the field-induced SMM behavior of four compounds. Without an external field, the frequency and temperature dependent on ac susceptibility signals of the out-of-phase (χ'') components for 1Dy and 2Dy cannot be found, whereas the χ'' signals for 3Dy and 4Dy bring out an apparent frequency dependence because of the slow magnetic relaxation. Because the reason for quantum tunnelling of magnetization (QTM) usually found in Ln-based SMMs decreased the anisotropy barriers, no peak maxima for four compounds are observed for χ'' above 2 K without a dc field. QTM primarily derives from the hyperfine interactions of Dy^{3+} nuclear spins at cryogenic temperatures; consequently, the intrinsic nature of Kramer's Dy^{3+} ions breaks down accompanied by the principle quantum number splitting in the low symmetrical configuration of Dy^{3+} ions.⁵¹ To circumvent any possible QTM effect, the different dc fields are applied in ac susceptibility measurements to remove the degeneracy of ground states. In order to seek the optimal dc field, the ac susceptibility measurements in different dc field range of 0–3000 Oe were carried out at 2 K. When raising the dc field from 0 to 3000 Oe, both the χ' and χ'' components gradually show frequency-dependent signals, the peaks maxima in the χ'' curves are distinctly observed appearing at 3000 Oe. This indicates the QTM is increasingly conquered under the predefined dc fields (Figures S10–S13, Supporting Information). When applying the optimum dc field around at 3 kOe, the looming peaks of χ'' susceptibility curves for 1Dy and the obvious χ'' peak signals for 2Dy–4Dy can be found below 15 K (Figure 5e–h). QTM can be significantly prevented under the optimum dc field, resulting in the relaxation is controlled by next fastest pathway like Orbach process, thereby causes the field-induced SMM behavior.⁵² For getting the energy barriers and the corresponding relaxation times, the incomplete semicircle shapes in the Cole–Cole diagrams are observed in a 3000 Oe dc field below 15 K between 50 and 999 Hz. The distribution coefficient α in the range of 0.53–0.63 are calculated on the basis of Debye model (Figure Si–1), indicating a thermally activated relaxation process in these systems accompanying with a narrow distribution of relaxation times. According to the Arrhenius plots [$\tau = \tau_0 \exp(U_{\text{eff}}/k_B T)$] for 1Dy–4Dy in the range of 3–6 K (Figure 5m–p), the calculated effective energy barriers and relaxation times are $U_{\text{eff}} = 55 \text{ K}$ and $\tau_0 = 9.6 \times 10^{-12} \text{ s}$ (1Dy), $U_{\text{eff}} = 57 \text{ K}$ and $\tau_0 = 1.5 \times 10^{-10} \text{ s}$ (2Dy), $U_{\text{eff}} = 37 \text{ K}$ and $\tau_0 = 4.4 \times 10^{-7} \text{ s}$ (3Dy), and $U_{\text{eff}} = 64 \text{ K}$ and $\tau_0 = 9.4 \times 10^{-10} \text{ s}$ (4Dy) respectively, which are

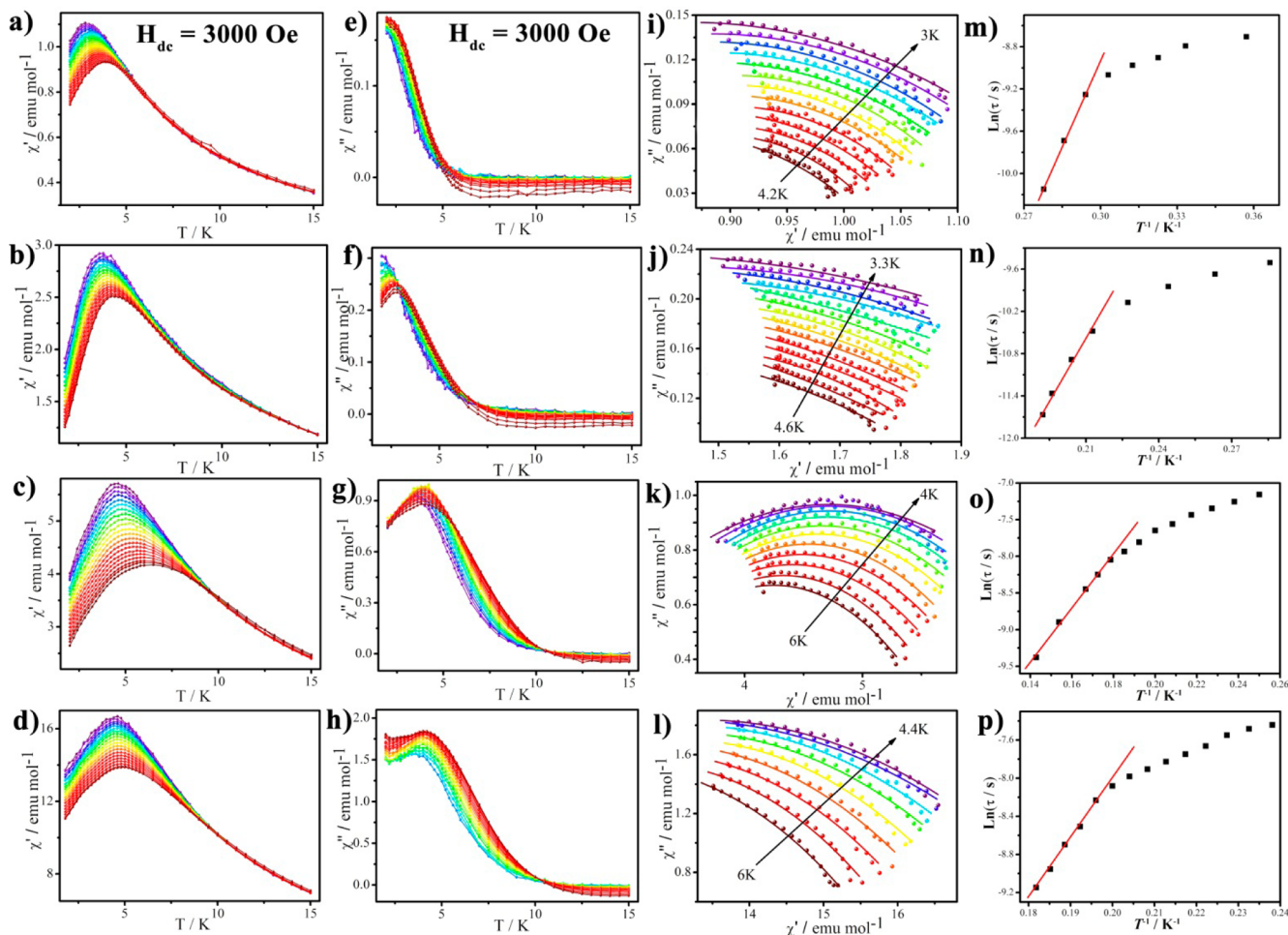


Figure 5. Temperature-dependent real components (χ') (a–d) and imaginary components (χ'') (e–h) of ac susceptibility signals at different frequencies under a 3 kOe dc field for **1Dy–4Dy**. (i–l) Cole–Cole plots of **1Dy–4Dy** with the solid rainbow lines represent the best fits to the experimental data. (m–p) Relaxation times as a function of the inverse temperature for **1Dy–4Dy**; the solid lines are fitted with Arrhenius law.

accordance with the anticipated energy gaps of 10^{-6} – 10^{-13} s for SMM behaviors.⁴⁹ As far as we know, these energy barriers are comparable with the previously reported Dy-containing POM-based SMMs,^{53,54} which are affected by the local symmetry of Dy^{3+} ions configurations, the ligand fields of Dy^{3+} ions, and the minute modification of the environment of magnetic molecules.

Further insight into the dynamic behaviors of **1Dy–4Dy** were studied by the measurement of the low temperature hysteresis loops. As shown in **Figures 6** and **S14**, the looming butterfly-shaped hysteresis loops are found for **1Dy** and **2Dy**, whereas the narrow butterfly-shaped hysteresis loop are clearly observed for **3Dy** and **4Dy** below 5 K between -10 and $+10$ kOe with a 500 Oe s^{-1} scan rate. This implies that the fast QTM is dominant in **1Dy** and **2Dy**, which is difficult to be suppressed by external dc fields. On lowering the temperature to 2 K, these butterfly-shaped hysteresis loops of **3Dy** and **4Dy** become much larger and wider at 2 K, which agrees well with the dominant QTM at low temperatures for Ln-based compounds.⁵⁵ When increasing the magnetic field, the loops become broader in the field range of 2–4 kOe, which are in accordance with the optimum dc field of 3 kOe. On the contrary, the loops become narrower and even disappear as the scan rate decreasing from 500 to 100 Oe s^{-1} , indicating more obvious QTM in **1Dy–4Dy** (**Figure S15**, **Supporting**

Information). The strong dynamic dependence of hysteresis loops toward the temperatures or scan rates is in accordance with the ac susceptibility results.

CONCLUSIONS

All in all, a series of Dy-based POMs crystalline materials embodied different lacunary Keggin-type phosphotungstates as host ligands have been synthesized and fully characterized, which display different structural features with the number of Dy^{3+} ions from mononuclearity, binuclearity, trinuclearity to octa-nuclearity. **1Dy–4Dy** clearly display characteristic emissions of the Dy^{3+} ions with the POM as an effective inorganic antenna due to the prominent $\text{O} \rightarrow \text{M}$ LMCT. Among them, **1Dy** displays the highest luminescent intensity and the longest lifetime regardless of the visible or NIR emission, resulting from its unique eight-coordinate square antiprism configuration of Dy^{3+} ion with no coordinated water ligands. Consequently, the luminescence of the Dy^{3+} ion is highly sensitized by the photoexcitation of POMs $\text{O} \rightarrow \text{W}$ LMCT; synchronously, the fluorescence quenching caused by the high frequency O–H oscillator under photoexcitation was effectively avoided. Static magnetic studies for **1Dy–4Dy** reveal that **1Dy–3Dy** show the progressive thermal depopulation of Dy^{3+} ions, whereas **4Dy** possess dominant ferromagnetic interactions between the Dy^{3+} ions in the low temperature as well as the depopulation of Dy^{3+}

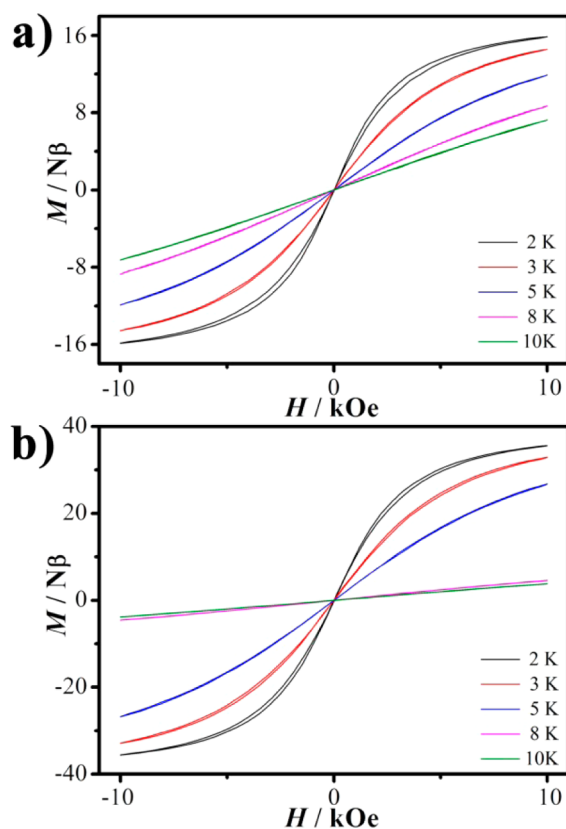


Figure 6. Hysteresis loops for 3Dy (a) and 4Dy (b) measured at 2–10 K.

Stark levels. The dynamic magnetic behaviors of 1Dy–4Dy exhibit thermal activated slow magnetic relaxation and the quantum tunnelling effect. Especially, 3Dy and 4Dy clearly show slow magnetic relaxation at 3 kOe and the observed hysteresis loops. In summary, the four compounds simultaneously displayed field-induced SMMs behaviors and the tunable photoluminescence behaviors, endowing them magneto-optical bifunctional properties. This research opens an avenue to synthesize the Ln-based POMs crystalline materials possessed both luminescence and SMMs properties by selecting the appropriate host ligands and Ln ions. In the next stage, we will devote ourselves to exploring novel Ln-based crystalline POMs multifunctional materials by the subtle assembly of the selective Ln ions with various POM units and the introduced functionalized organic ligands, thereby greatly enriching the versatility of Ln-based crystalline POMs materials.

■ ASSOCIATED CONTENT

Supporting Information

The Supporting Information is available free of charge on the ACS Publications website at DOI: 10.1021/acs.cgd.6b01895.

Photoluminescence excitation spectra, IR spectra, XRD diffractograms, TGA curves, magnetic curves, EDX spectra, and related structural figures; crystal data (PDF)

Accession Codes

CCDC 1521758–1521761 contains the supplementary crystallographic data for this paper. These data can be obtained free of charge via www.ccdc.cam.ac.uk/data_request/cif, or by

emailing data_request@ccdc.cam.ac.uk, or by contacting The Cambridge Crystallographic Data Centre, 12, Union Road, Cambridge CB2 1EZ, UK; fax: +44 1223 336033.

■ AUTHOR INFORMATION

Corresponding Authors

*E-mail: jyniu@henu.edu.cn.

*E-mail: jpwang@henu.edu.cn. Fax: (+86) 371 23886876.

ORCID

Jingyang Niu: 0000-0001-6526-7767

Notes

The authors declare no competing financial interest.

■ ACKNOWLEDGMENTS

This work was financially supported by the NSFC and the Natural Science Foundation of Henan Province (132300410144, 162300410015).

■ REFERENCES

- (1) Saad, A.; Oms, O.; Marrot, J.; Dolbecq, A.; Hakouk, K.; El Bekkachi, H.; Jobic, S.; Deniard, P.; Dessapt, R.; Garrot, D.; Boukheddaden, K.; Liu, R.; Zhang, G.; Keita, B.; Mialane, P. *J. Mater. Chem. C* **2014**, *2*, 4748.
- (2) Li, J.-S.; Sang, X.-J.; Chen, W.-L.; Zhang, L.-C.; Zhu, Z.-M.; Ma, T.-Y.; Su, Z.-M.; Wang, E.-B. *ACS Appl. Mater. Interfaces* **2015**, *7*, 13714.
- (3) Dolbecq, A.; Dumas, E.; Mayer, C. R.; Mialane, P. *Chem. Rev.* **2010**, *110*, 6009.
- (4) Blum, A. P.; Kammeyer, J. K.; Rush, A. M.; Callmann, C. E.; Hahn, M. E.; Gianneschi, N. C. *J. Am. Chem. Soc.* **2015**, *137*, 2140.
- (5) Rinehart, J. D.; Long, J. R. *Chem. Sci.* **2011**, *2*, 2078.
- (6) Jerome, L.; Vallat, R.; Ferreira, R. A. S.; Carlos, L. D.; Almeida Paz, F. A.; Guari, Y.; Larionova, J. *Chem. Commun.* **2012**, *48*, 9974.
- (7) Cucinotta, G.; Perfetti, M.; Luzon, J.; Etienne, M.; Car, P.-E.; Caneschi, A.; Calvez, G.; Bernot, K.; Sessoli, R. *Angew. Chem., Int. Ed.* **2012**, *51*, 1606.
- (8) Mohapatra, S.; Rajeswaran, B.; Chakraborty, A.; Sundaresan, A.; Maji, T. K. *Chem. Mater.* **2013**, *25*, 1673.
- (9) Pope, M.-T. *Heteropoly and Isopoly Oxometalates*; Springer-Verlag: Berlin, 1983.
- (10) Han, Q.; Sun, X.; Li, J.; Ma, P.; Niu, J. *Inorg. Chem.* **2014**, *53*, 6107.
- (11) Gao, N.; Sun, H.; Dong, K.; Ren, J.; Duan, T.; Xu, C.; Qu, X. *Nat. Commun.* **2014**, *5*, 3422.
- (12) Omwoma, S.; Gore, C. T.; Ji, Y.; Hu, C.; Song, Y.-F. *Coord. Chem. Rev.* **2015**, *286*, 17.
- (13) Xu, L.; Zhang, H.; Wang, E.; Kurth, D. G.; Li, Z. *J. Mater. Chem.* **2002**, *12*, 654.
- (14) Li, H.; Qi, W.; Li, W.; Sun, H.; Bu, W.; Wu, L. *Adv. Mater.* **2005**, *17*, 2688.
- (15) Ritchie, C.; Moore, E. G.; Speldrich, M.; Kögerler, P.; Boskovic, C. *Angew. Chem., Int. Ed.* **2010**, *49*, 7702.
- (16) Zhao, W.-F.; Zou, C.; Shi, L.-X.; Yu, J.-C.; Qian, G.-D.; Wu, C.-D. *Dalton Trans.* **2012**, *41*, 10091.
- (17) Yamase, T.; Kobayashi, T.; Sugeta, M.; Naruke, H. *J. Phys. Chem. A* **1997**, *101*, 5046.
- (18) Yamase, T. *Chem. Rev.* **1998**, *98*, 307.
- (19) Leuenberger, M. N.; Loss, D. *Nature* **2001**, *410*, 789.
- (20) Gatteschi, D.; Sessoli, R.; Villain, J. *Molecular Nanomagnets*; Oxford University Press: Oxford, 2006.
- (21) Vincent, R.; Klyatskaya, S.; Ruben, M.; Wernsdorfer, W.; Balestro, F. *Nature* **2012**, *488*, 357.
- (22) Ruiz, E.; Cirera, J.; Cano, J.; Alvarez, S.; Loose, C.; Kortus, J. *Chem. Commun.* **2008**, 52.
- (23) Guo, Y.-N.; Xu, G.-F.; Guo, Y.; Tang, J. *Dalton Trans.* **2011**, *40*, 9953.

- (24) AlDamen, M. A.; Clemente-Juan, J. M.; Coronado, E.; Martí-Gastaldo, C.; Gaita-Ariño, A. *J. Am. Chem. Soc.* **2008**, *130*, 8874.
- (25) Ritchie, C.; Speldrich, M.; Gable, R. W.; Sorace, L.; Kögerler, P.; Boskovic, C. *Inorg. Chem.* **2011**, *50*, 7004.
- (26) Cardona-Serra, S.; Clemente-Juan, J.-M.; Coronado, E.; Gaita-Ariño, A.; Camón, A.; Evangelisti, M.; Luis, F.; Martínez-Pérez, M.-J.; Sese, J. *J. Am. Chem. Soc.* **2012**, *134*, 14982.
- (27) Suzuki, K.; Sato, R.; Mizuno, N. *Chem. Sci.* **2013**, *4*, 596.
- (28) Ma, P.; Wan, R.; Si, Y.; Hu, F.; Wang, Y.; Niu, J.; Wang, J. *Dalton Trans.* **2015**, *44*, 11514.
- (29) Ma, P.; Hu, F.; Wan, R.; Huo, Y.; Zhang, D.; Niu, J.; Wang, J. *J. Mater. Chem. C* **2016**, *4*, 5424.
- (30) Tourne, C. M.; Tourne, G. F. *J. Chem. Soc., Dalton Trans.* **1988**, 2411.
- (31) Pradeep, C. P.; Long, D.-L.; Cronin, L. *Dalton Trans.* **2010**, *39*, 9443.
- (32) Sheldrick, G. M. *Acta Crystallogr., Sect. A: Found. Crystallogr.* **2008**, *64*, 112.
- (33) Zhang, S.; Zhang, D.; Ma, P.; Liang, Y.; Wang, J.; Niu, J. *CrystEngComm* **2013**, *15*, 2992.
- (34) Niu, J.; Wang, K.; Chen, H.; Zhao, J.; Ma, P.; Wang, J.; Li, M.; Bai, Y.; Dang, D. *Cryst. Growth Des.* **2009**, *9*, 4362.
- (35) Suzuki, K.; Sugawa, M.; Kikukawa, Y.; Kamata, K.; Yamaguchi, K.; Mizuno, N. *Inorg. Chem.* **2012**, *51*, 6953.
- (36) Wang, J.-P.; Zhao, J.-W.; Duan, X.-Y.; Niu, J.-Y. *Cryst. Growth Des.* **2006**, *6*, 507.
- (37) Gupta, R.; Saini, M. K.; Doungmene, F.; de Oliveira, P.; Hussain, F. *Dalton Trans.* **2014**, *43*, 8290.
- (38) Gupta, R.; Saini, M. K.; Hussain, F. *Eur. J. Inorg. Chem.* **2014**, *2014*, 6031.
- (39) Howell, R. C.; Perez, F. G.; Jain, S.; DeW. Horrocks, J. W.; Rheingold, A. L.; Francesconi, L. C. *Angew. Chem., Int. Ed.* **2001**, *40*, 4031.
- (40) Li, F.; Guo, W.; Xu, L.; Ma, L.; Wang, Y. *Dalton Trans.* **2012**, *41*, 9220.
- (41) Richardson, F. S. *Chem. Rev.* **1982**, *82*, 541.
- (42) Butünzli, J. C. G.; Piguët, C. *Chem. Soc. Rev.* **2005**, *34*, 1048.
- (43) Mahata, P.; Ramya, K. V.; Natarajan, S. *Chem. - Eur. J.* **2008**, *14*, 5839.
- (44) Zhang, Y.; Gong, W. T.; Yu, J. J.; Pang, H. C.; Song, Q.; Ning, G. L. *RSC Adv.* **2015**, *5*, 62527.
- (45) Wu, L.; Zhang, Y.; Gui, M. Y.; Lu, P. Z.; Zhao, L. X.; Tian, S.; Kong, Y. F.; Xu, J. J. *J. Mater. Chem.* **2012**, *22*, 6463.
- (46) Feng, J.; Zhang, H.-J.; Song, S.-Y.; Li, Z.-F.; Sun, L.-N.; Xing, Y.; Guo, X.-M. *J. Lumin.* **2008**, *128*, 1957.
- (47) Feng, X.-J.; Han, H.-Y.; Wang, Y.-H.; Li, L.-L.; Li, Y.-G.; Wang, E.-B. *CrystEngComm* **2013**, *15*, 7267.
- (48) Ahmed, Z.; Iftikhar, K. *Inorg. Chem.* **2015**, *54*, 11209.
- (49) Calahorra, A. J.; Oyarzabal, I.; Fernandez, B.; Seco, J. M.; Tian, T.; Fairen-Jimenez, D.; Colacio, E.; Rodriguez-Dieguez, A. *Dalton Trans.* **2016**, *45*, 591.
- (50) Xiang, H.; Lan, Y.; Li, H.-Y.; Jiang, L.; Lu, T.-B.; Anson, C.-E.; Powell, A.-K. *Dalton Trans.* **2010**, *39*, 4737.
- (51) Yin, D.-D.; Chen, Q.; Meng, Y.-S.; Sun, H.-L.; Zhang, Y.-Q.; Gao, S. *Chem. Sci.* **2015**, *6*, 3095.
- (52) Giansiracusa, M. J.; Vonci, M.; Van den Heuvel, W.; Gable, R. W.; Moubaraki, B.; Murray, K. S.; Yu, D.; Mole, R. A.; Soncini, A.; Boskovic, C. *Inorg. Chem.* **2016**, *55*, 5201.
- (53) Sawada, Y.; Kosaka, W.; Hayashi, Y.; Miyasaka, H. *Inorg. Chem.* **2012**, *51*, 4824.
- (54) Fang, X.; Kögerler, P.; Speldrich, M.; Schilder, H.; Luban, M. *Chem. Commun.* **2012**, *48*, 1218.
- (55) Chen, Q.; Meng, Y.-S.; Zhang, Y.-Q.; Jiang, S.-D.; Sun, H.-L.; Gao, S. *Chem. Commun.* **2014**, *50*, 10434.